PCCP

Reaction Uniformity Visualized by Raman Imaging in Composite Electrode Layers of All-Solid-State Lithium Batteries

Journal:	*Physical Chemistry Chemical Physics*
Manuscript ID	CP-ART-01-2020-000508.R2
Article Type:	Paper
Date Submitted by the Author:	29-Apr-2020
Complete List of Authors:	Otoyama, Misae ; Osaka Prefecture University, Applied Chemistry Ito, Yusuke ; Osaka Prefecture University, Applied Chemistry Sakuda, Atsushi; Osaka Prefecture University, Department of Applied Chemistry, Graduate School of Engineering Tatsumisago, Masahiro; Osaka Prefecture University, Applied Chemistry Hayashi, Akitoshi; Osaka Prefecture University, Applied Chemistry

ARTICLE

Reaction Uniformity Visualized by Raman Imaging in Composite Electrode Layers of All-Solid-State Lithium Batteries

Received 00th January 20xx,
Accepted 00th January 20xx

DOI: 10.1039/x0xx00000x

Misae Otoyama,[a] Yusuke Ito,[a] Atsushi Sakuda,[a] Masahiro Tatsumisago[a] and Akitoshi Hayashi*[a]

The reaction uniformity of $LiCoO_2$ composite positive electrodes in all-solid-state cells was compared quantitatively by investigating the Raman band shifts corresponding to the state-of-charge (SOC) of $LiCoO_2$. The quantitative SOC analysis was conducted for the Raman imaging data of composite electrodes with smaller or larger solid electrolytes. The electrodes exhibited different reaction uniformity although the cells showed the similar initial charge capacities and average SOC. In the case of larger solid electrolytes, most of $LiCoO_2$ particles showed higher or lower SOC than average SOC, and lower battery performance. The quantitative analysis of SOC in each $LiCoO_2$ demonstrated that a variable SOC outside the average SOC resulted in larger irreversible capacity and lower rate performance. The quantitative SOC analysis developed newly in the present study is a useful technique for designing composite electrodes showing higher battery performance.

1. Introduction

To accommodate the huge demand for alternative electric power sources that can replace fossil fuels, it is necessary to develop lithium ion batteries with high energy density.[1] All-solid-state batteries (ASSLBs) are anticipated to be the next-generation batteries due to their higher safety and theoretical energy density compared to the conventional lithium-ion batteries.[2] Bulk-type ASSLBs typically use composite electrodes consisting of electrode active materials and solid electrolytes (SEs).[3] Currently, the most significant issue for the development and commercial use of ASSLBs is that solid-solid interfaces and pores in the electrodes limit Li^+ ion and/or electron conduction paths, resulting in the deterioration of the battery performance.[4,5] Many experimental and computational studies have attempted to optimize the composite electrodes in order to overcome this issue.[6-17] To increase the effective contact area between the SEs and electrode active materials, the sizes of the SE and electrode active material particles have been decreased[6-9] and electrode active materials coated with a thin SE layer have been developed.[10-16] Kim *et al.* recently prepared compositionally graded composite electrodes consisting of three layers with different composition ratios of electrode active materials and SEs.[17] These approaches improved battery performance compared to the un-optimized electrodes. However, the experimental investigations performed to date have generally focused on only battery performance characteristics.[6-14,16,17] For the further optimization of composite electrodes, it is important to understand the reaction distributions in composite electrodes that are related to the Li^+ ion and electron conduction paths, because an inhomogeneous reaction distribution may give rise to side reactions.

In our previous reports, reaction distributions in composite positive electrodes with larger and smaller SE particles were investigated by Raman imaging.[18,19] We revealed that an inhomogeneous reaction distribution was formed in cells with the larger SEs due to the insufficient contact between the SEs and the electrode active materials. However, quantitative analyses of the reaction distributions in composite electrodes have not been performed. Introducing reaction uniformity as a parameter for the characterization of these materials may help the optimization of composite electrodes.

In the present study, a quantitative analysis of the state-of-charge (SOC) of $LiCoO_2$ electrodes was carried out for the composite electrodes with larger and smaller SE particles. The same cells examined already for Raman imaging[18,19] were used for studying reaction uniformity quantitatively. Advanced analysis on Raman imaging was conducted by considering the peak shifts of the Raman band of $LiCoO_2$. We investigated the relationship between the capacities and reaction uniformities of the cells. It was revealed that reaction distributions were completely different even though the initial charge capacities of the cells were similar, and the difference in reaction uniformity affected the reversible capacity and rate performance of the cells.

2. Experimental

2.1. Preparation of solid electrolytes

[a] *Department of Applied Chemistry, Graduate School of Engineering, Osaka Prefecture University, 1-1, Gakuen-cho, Naka-ku, Sakai, Osaka 599-8531, Japan*

† Electronic supplementary information (ESI) available: fractions of high and low SOC areas and by-products; Raman spectral changes at the different capacities; and enlarged Raman mapping images. See DOI: 10.1039/x0xx00000x

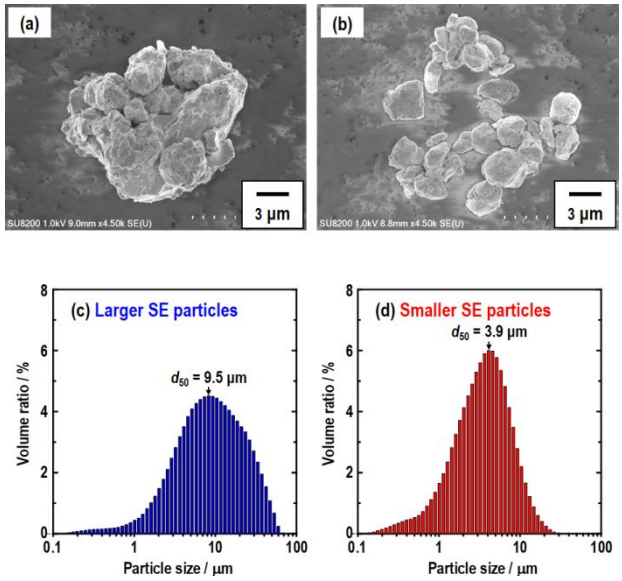

Fig. 1 SEM images of (a) larger and (b) smaller SE particles. Particle size distributions of (c) larger and (d) smaller SE particles.

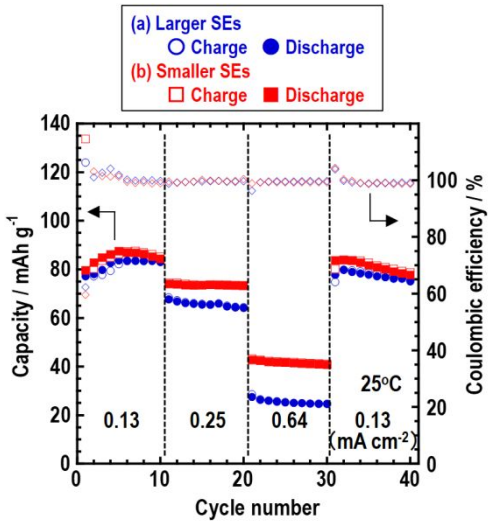

Fig. 2 Cycle performances and coulombic efficiency of all-solid-state cells using (a) larger or (b) smaller SE particles. The cells were cycled under the current densities of 0.13, 0.25, 0.64 and 0.13 mA cm^{-2} at 25°C with a cut-off voltage of 2.6–4.2 V (vs. Li^+/Li).

The $75Li_2S{\cdot}25P_2S_5$ (mol%) glass SE particles were prepared by mechanochemical treatment of Li_2S (Idemitsu Kosan, 99.9%) and P_2S_5 (Aldrich, 99%) crystalline powders. The batches (1 g) of these mixtures with the composition of $75Li_2S{\cdot}25P_2S_5$ (mol%) were placed into a zirconia pot (45 mL in volume) with 500 zirconia balls (4 mm in diameter). The zirconia pots were mechanically milled at 510 rpm for 45 hours using a planetary ball mill (Pulverisette 7; Fritsch). To compare the battery performance characteristics of the cells using composite electrodes with SEs of different particle size, smaller $75Li_2S{\cdot}25P_2S_5$ glass SE particles were obtained by a wet mechanical milling technique with heptane and dibutyl ether.[20]

To compare particle sizes of larger and smaller SEs, scanning electron microscopy (SEM) (SU8220; HITACHI) observation was conducted. Particle distributions were examined by using a nano particle size analyzer (SALD-7500nano; SHIMADZU). Anisole (30 mg) and tributylamine (6.585 mg) were mixed as solvent and then poured into a quartz cell. After blank measurement, SEs were put into the cell and their particle distributions were measured.

2.2. Fabrication of all-solid-state cells

To compare reaction distributions, larger and smaller $75Li_2S{\cdot}25P_2S_5$ glass SE particles were used in composite positive electrodes. Composite electrodes were prepared by mixing $LiNbO_3$-coated $LiCoO_2$ particles (diameter in *ca.* 10 μm) and the larger or smaller $75Li_2S{\cdot}25P_2S_5$ glass SE particles with a weight ratio of 80/20. A $LiNbO_3$ buffer layer decreases the interfacial resistance between $LiCoO_2$ and sulfide SEs.[21] Larger $75Li_2S{\cdot}25P_2S_5$ glass SEs (40 mg) were pressed slightly to prepare a SE separator layer. A bilayer pellet was obtained by placing the composite positive electrode (10 mg) on the SE separator layer and pressing under 360 MPa. An indium foil (99.999%; Furuuchi Chemical Corp.) as a counter electrode was then attached to the bilayer pellet and pressed with stainless steel powder (SUS304L, Kojundo Chemical) (100 mg) as a current collector under 240 MPa. A pellet (8 mm × 4 mm × 2 mm^t) was sandwiched by two stainless-steel plates as current collectors.

For the cycle tests, another type cell (diameter in 10 mm) was constructed. The larger $75Li_2S{\cdot}25P_2S_5$ glass SE particles (80 mg) were pressed to obtain a SE separator layer. The $LiCoO_2$ composite positive electrode (10 mg) was put on the SE layer and then pressed at 360 MPa. An indium foil (Φ = 9 mm) was attached to the bilayer pellet as a counter electrode and pressed at 240 MPa. The pellets were pressed with two stainless steel disks as current collectors. All the processes for preparation of SEs and fabrication of all-solid-state cells were conducted at room temperature in a dry Ar-filled glove box.

The cells were charged and discharged with the cut-off voltage of 2.6–4.2 V (vs. Li^+/Li) at 25°C under a current density of 0.064, 0.13, 0.25, 0.64 mA cm^{-2} using a charge-discharge measuring device (BTS-2004; Nagano Co Ltd., Japan). AC impedance measurements were conducted for the cells after the cycle tests using an impedance analyzer (SI 1260 and SI 1278; Solartoron).

2.3. Raman imaging

After the initial charge and discharge tests, the layered pellet of In|$75Li_2S{\cdot}25P_2S_5$ (mol%) glass|$LiCoO_2$ was dismounted from the cells. To remove irregularities on the surface and prepare flat samples, cross-sections of the electrodes were polished by an Ar ion-milling technique using an ion-milling system (IM4000; HITACHI). After that, the pellets were sealed in a container with an optical flat glass window and O-rings in a dry Ar-filled globe box. Raman imaging was performed for the surface part of the positive electrodes after the initial charge and discharge tests using a Raman microscope (RAMANtouch; nanophoton). The laser beam was focused onto the samples using a 50× objective (NA = 0.70, Nikon) with excitation at 532 nm. The intensity of the laser beam was *ca.* 10^4~10^6 W cm^{-2}. Spatial and depth resolutions were *ca.* 1.6 μm and *ca.* 2–3 μm,

respectively. Before conducting Raman imaging, SEM observation was conducted for the cross-sections of the electrodes prepared by Ar ion-milling technique.

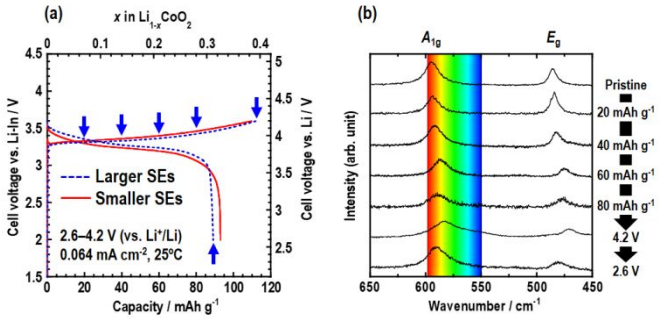

Fig. 3 (a) Initial charge-discharge curves of the all-solid-state cells with larger SE particles and smaller SE particles used for Raman imaging. The cells operated under a current density of 0.064 mA cm^{-2} at 25°C with a cut-off voltage of 2.6–4.2 V (vs. Li^+/Li). (b) Raman spectra of the $LiCoO_2$ composite positive electrodes with larger SE particles at different charge-discharge capacities. The Raman spectra were collected for the pristine cell and the cell charged to 20, 40, 60, and 80 mAh g^{-1} and 4.2 V (vs. Li^+/Li), and discharged to 2.6 V (vs. Li^+/Li), as indicated by blue arrows in Fig. 3a.

3. Results and discussion

Fig. 1 shows the SEM images and particle size distributions of the larger and smaller SEs. The particle sizes of the larger SEs (d_{50} = 9.5 µm) and smaller SEs (d_{50} = 3.9 µm) were different by a factor of more than two. The size of primary particles of larger and smaller SEs were similar, and larger SEs consisted of secondary particles formed by agglomerated primary particles. The Li ion conductivity of both the SEs was almost the same ($2\sim3\times10^{-4}$ S cm^{-1} at 25°C). Fig. 2 shows cycle performance under various current densities of the cells using $LiCoO_2$ composite positive electrodes with larger and smaller SE particles. Coulombic efficiency of the cells was almost 100% except for the initial cycle. The cells operated reversibly from the 2nd cycle. Fig. S1 in the ESI † shows the 10th, 20th, and 30th charge-discharge curves of the cells under the current densities of 0.13 mA cm^{-2}, 0.25 mA cm^{-2}, and 0.64 mA cm^{-2}. At 0.13 mA cm^{-2}, capacities of the cells were similar, while the cell with larger SEs showed higher polarization and lower capacity at 0.64 mA cm^{-2}. Impedance measurements were conducted for the cells after the 40th discharging process (Fig. S2 in the ESI †). The cell with the larger SEs exhibited a larger resistance and lower rate performance, suggesting that insufficient contacts between $LiCoO_2$ and SE particles brought about larger resistances during the cycle test, and degraded battery performance, especially at high current density.

Raman imaging was conducted for the composite electrode layers after the initial charge and discharge tests. Figs. 3a and 3b show the initial charge-discharge curves of the cells with larger and smaller SEs used for Raman imaging, and Raman spectral changes of the $LiCoO_2$ electrodes in ASSLBs at the different SOC, respectively. The Raman spectra were collected for the pristine cell and the cells charged to 20, 40, 60, and 80 mAh g^{-1} and 4.2 V (vs. Li^+/Li), and discharged to 2.6 V (vs. Li^+/Li). As we reported in the refs. 18 and 19, E_g and A_{1g} bands of $LiCoO_2$ shift to the lower wave number side during the charge test and shift to the original positions during the discharge test. In the present study, we newly evaluated peak positions of the A_{1g} band in detail. To describe rainbow color bars for Raman imaging corresponding to the Raman spectral changes, we used the same Raman spectra reported in refs. 18 and 19. In our previous study of the Raman imaging of charged and discharged electrode layers, we defined $LiCoO_2$ with low SOC and high SOC, SEs and Co_3O_4 (by-product at overcharging) with four colors by using the differences in the peak positions of Raman bands.[18,19] Except for the SE areas, abundance ratio was calculated by an area analysis for the Raman mapping images and the obtained results are summarized in Table S1 in the ESI † . For the larger SEs, low SOC areas remained after the discharge test, and Co_3O_4 formed after the charge-discharge tests. On the other hand, the SOC changed reversibly and Co_3O_4 did not form in the cells with the smaller SEs, suggesting that reversible charge-discharge reactions proceeded without side reactions.

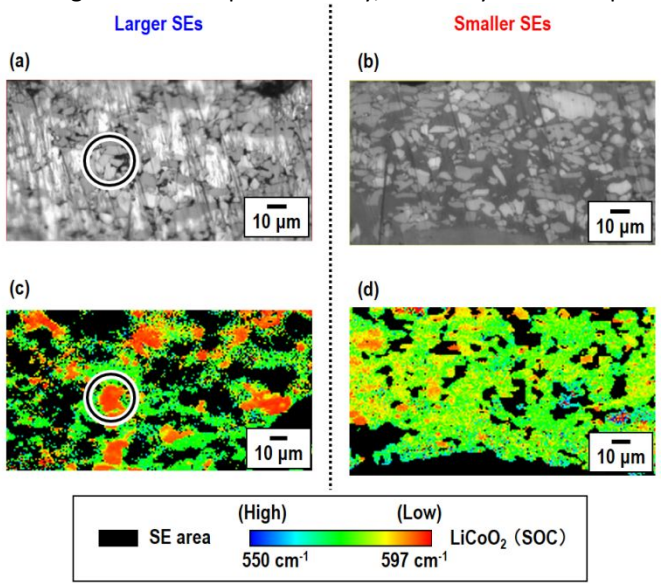

Fig. 4 Optical micrographs of the charged $LiCoO_2$ electrodes using (a) larger and (b) smaller SE particles republished from refs. 18 and 19. Raman mapping images for the micrographs of (a) and (b) are shown as (c) and (d), respectively. Black circles show aggregated $LiCoO_2$. Advanced analysis was conducted with rainbow colors for the Raman mapping images published in refs. 18 and 19.

In the present study, we focused on the quantitative analysis for SOC of $LiCoO_2$, and investigated the peak positions of the A_{1g} mode highlighted with rainbow colors in the range of 550 cm^{-1} and 597 cm^{-1} in Fig. 3b. Fig. S3 in the ESI † shows the Raman spectra of $LiCoO_2$ with various SOCs mapped onto a rainbow color index. In this analysis, high SOC areas with low wavenumber are colored either green or blue. Fig. 4 shows the optical micrographs and corresponding Raman mapping images with a rainbow color map of the composite positive electrodes using larger or smaller SE particles after the charge test. In this study, advanced analysis with rainbow colors was conducted for the same cells examined in refs. 18 and 19. The optical micrographs of the cells were the same figures published in refs. 18 and 19, while the Raman mapping images

ARTICLE

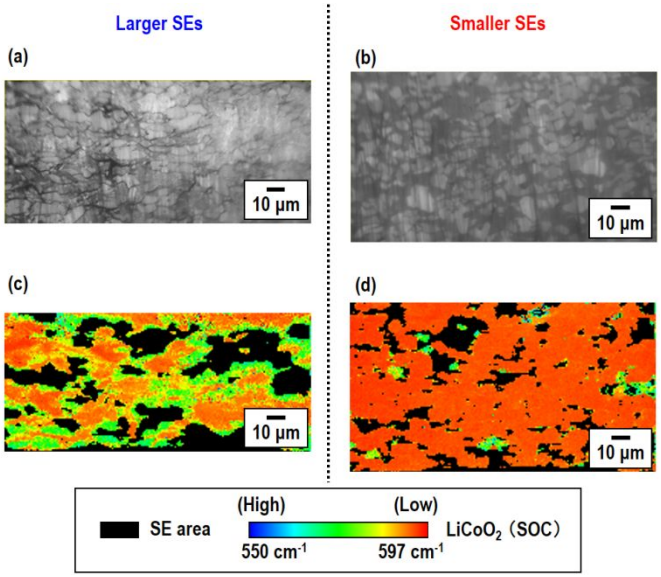

Fig. 5 Optical micrographs of the discharged $LiCoO_2$ electrodes using (a) larger and (b) smaller SE particles republished from ref. 19. Raman mapping images for the micrographs of (a) and (b) are shown as (c) and (d), respectively. Advanced analysis was conducted with rainbow colors for the Raman mapping images published in ref. 19.

with rainbow colors were new data. SE areas are colored black. Larger amounts of the low SOC areas colored red were observed in the electrode using larger SEs (Figs. 4a and c). Low SOC areas were particularly often observed in the aggregated $LiCoO_2$ highlighted by black circles. Focusing on the interfaces between $LiCoO_2$ and SEs (Fig. S4 in the ESI †), high SOC areas colored blue were observed, indicating that some of $LiCoO_2$ at the interfaces were easily delithiated. For the smaller SEs, most $LiCoO_2$ particles were colored green, indicating that they exhibited almost the same SOC (Figs. 4b and d).

Fig. 5 shows the optical micrographs and corresponding Raman mapping images with rainbow colors of the composite positive electrodes using larger or smaller SE particles after the discharge test. When smaller SEs were used, most of $LiCoO_2$ was in the discharged state with low SOC colored red. This indicates that a uniform reaction distribution was achieved. On the other hand, in the cell with the larger SEs, charged $LiCoO_2$ remained at the interfaces between $LiCoO_2$ and SEs, and the discharge reaction proceeded in the limited areas. High SOC areas colored blue were observed at the interfaces in Fig. S5 in the ESI †, indicating that irreversible reactions occurred at the interfaces. Use of smaller SEs increases the area of contact between $LiCoO_2$ and SEs, and gives rise to a uniform reaction distribution in the composite electrodes. According to the quantitative analysis of the SOC distribution, some regions of the $LiCoO_2$ particles near the interfaces between $LiCoO_2$ and larger SEs were easily delithiated and high SOC areas remained even after the discharge test.

A further analysis of the SOC distribution was performed using histograms of the peak positions of the A_{1g} mode. Fig. 6 shows the histograms of the peak positions of the A_{1g} mode, and it is observed that they correspond to the SOC values of $LiCoO_2$.[18,22,23] For the larger SEs, most of the peaks were at 593

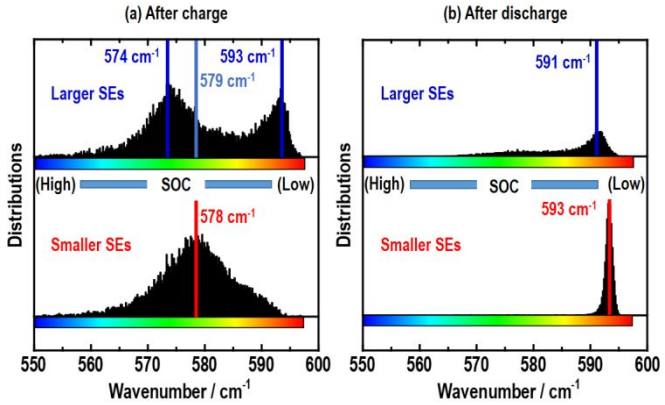

cm^{-1} and 574 cm^{-1}, corresponding to x = *ca.* 0.1 and x = *ca.* 0.5

Fig. 6 Histogram of the peak positions of the A_{1g} mode of the $LiCoO_2$ electrode layers using (a) larger or (b) smaller SE particles after the (a) charge and (b) discharge tests.

in $Li_{1-x}CoO_2$, respectively. For the smaller SEs, a single distribution peak at 578 cm^{-1} was observed corresponding to x = *ca.* 0.4. The average peak positions of the cells with the larger and smaller SEs were similar, at 579 cm^{-1} and 578 cm^{-1}, respectively. These values correspond to the charge capacity of approximately 110 mAh g^{-1}. In the present study, the charge capacities of the cells were 117 mAh g^{-1} for the larger SEs and 107 mAh g^{-1} for the smaller SEs. Although the charge capacities of both cells are almost the same, quantitative SOC evaluation revealed that high and low SOC groups existed separately in the cell with the larger SEs as shown in Fig. 6a. This is related to the fact that the by-product, Co_3O_4, was formed only in the cells using the larger SEs, because Co_3O_4 is formed when the cells are overcharged and have a high SOC. Fig. 6b shows the histogram of the discharged cells. Unlike for the smaller SEs, for the larger SEs, some peaks remained at high SOC and almost all of the peaks did not return to their original positions. This is related to the lower coulombic efficiency of 79% observed for the cell with the larger SEs compared to that of the cell with the smaller SEs of 85%. Based on the quantitative analysis, the SOC distributions in the composite electrodes were investigated; such distributions cannot be deduced from battery capacity measurements only. One of the causes of the by-product formation was that some $LiCoO_2$ regions have higher SOC that is greater than the average SOC after the charge test. It is likely that the higher SOC areas were formed by current concentrations due to inhomogeneous conduction paths, and higher SOC areas induced side reactions such as local overcharging. Fig. S1 in the ESI † shows that the difference of polarization between the cells with larger and smaller SEs is larger at 0.64 mA cm^{-2} compared with 0.13 mA cm^{-2}. The cell with larger SEs showed lower capacities at 0.64 mA cm^{-2}. In other words, composite positive electrode with larger SEs had a larger amount of electrochemically inactive $LiCoO_2$ particles. Because both cells showed similar capacity at 0.13 mA cm^{-2} (Fig. 3 (a) and Fig. S1 (a)), electrochemically active $LiCoO_2$ particles were partially overcharged in the cell with larger SEs, and by-product Co_3O_4 was formed. Therefore, low reaction uniformity results in by-product formation and degradation of reversibility and rate performance. It is important to distinguish electrochemically active and inactive

$LiCoO_2$ particles in composite electrodes for improving morphology of electrodes. Liu *et al* have investigated ionic and electronic tortuosity, and compared them in the conventional and optimized electrodes.[24] To understand suitable design of composite electrode, calculating tortuosity, and evaluating electrochemical activity of electrode active materials is informative, and our focus of future research.

4. Conclusions

Quantitative SOC analysis for Raman imaging data newly evaluated here is useful for evaluating SOC of each $LiCoO_2$ particle in the composite positive electrode. In our previous study, we mentioned that the use of smaller SEs in composite electrodes led to uniform reaction distributions compared with larger SEs by qualitative (non-quantitative) Raman imaging based on the four colors for high SOC $LiCoO_2$, low SOC $LiCoO_2$, SE and by-product. In this study, we have concluded that monitoring the distribution of low SOC $LiCoO_2$ particles by visualization based on quantitative analysis is significant for predicting the extent of uniform electrochemical reactions in composite electrodes. Comparing the $LiCoO_2$ electrodes with larger and smaller SE particles, quantitative SOC distributions showed that the average SOCs of both composite electrodes were similar. This is related to the almost identical charge capacities observed for both composite electrodes. In contrast, some areas showed higher and lower SOC $LiCoO_2$ compared to the average SOC in the composite with the larger SEs, resulting in the formation of by-products at overcharging. Moreover, after the discharging process, the SOC of $LiCoO_2$ did not change reversibly in the composite electrodes with larger SEs, corresponding to their lower coulombic efficiency. Therefore, the quantitative SOC distribution analysis clearly revealed that reaction uniformity was different even though similar capacities were observed. Low reaction uniformity contributed low coulombic efficiency and rate performance. Quantitative analysis developed in this study is an important clue to designing composite electrodes for realizing high coulombic efficiency and good rate performance in solid-state batteries.

Conflicts of interest

There are no conflicts to declare.

Acknowledgements

This research was supported by JST ALCA-SPRING Grant Number JPMJAL1301, Japan, and by JSPS KAKENHI Grant Number 18H05255. Raman imaging and analysis were supported by Mr. Yusuke Shiozaki (Nanophoton corp.).

References

1 D. Larcher and J.-M. Tarascon, *Nat. Chem.*, 2015, **7**, 19–29.
2 A. Hayashi, A. Sakuda and M. Tatsumisago, *Front. Energy. Res*., 2016, **4,** 25.
3 T. Minami, A. Hayashi and M. Tatsumisago, *Solid State Ionics,* 2006, **177**, 2715–2720.
4 D. Hlushkou, A. E. Reising, N. Kaiser, S. Spannenberger, S. Schlabach, Y. Kato, B. Roling and U. Tallarek, *J. Power Sources*, 2018, **396**, 363–370.
5 A. Bielefeld, D. A. Weber and J. Janek, *J Phys. Chem. C*, 2019, **123**, 1626–1634
6 A. Sakuda, T. Takeuchi and H. Kobayashi, *Solid State Ionics*, 2016, **285**, 112–117.
7 S. Noh, W. T. Nichols, C. Park and D. Shin, *Ceram. Int.*, 2017, **43**, 15952–15958.
8 F. Strauss, T. Bartsch, L. D. Biasi, A-Y. Kim, J. Janek, P. Hartmann and T. Brezesinski, *ACS Energy Lett.*, 2018, **3**, 992–996.
9 T. Shi, Q. Tu, Y. Tian, Y. Xiao, L. J. Miara, O. Kononova and G. Ceder, *Adv. Energy Mater.*, 2019, 1902881.
10 A. Sakuda, A. Hayashi, T. Ohtomo, S. Hama and M. Tatsumisago, *J. Power Sources*, 2011, **196**, 6735–6741.
11 Y. Ito, A. Sakuda, T. Ohtomo, A. Hayashi and M. Tatsumisago, *Solid State Ionics*, 2013, **236**, 1–4.
12 S. Yubuchi, S. Teragawa, K. Aso, K. Tadanaga, A. Hayashi and M. Tatsumisago, *J. Power Sources*, 2015, **293**, 941–945.
13 K. H. Park, D. Y. Oh, Y. E. Choi, Y. J. Nam, L. Han, J.-Y. Kim, H. Xin, F. Lin, S. M. Oh and Y. S. Jung, *Adv. Mater.*, 2016, **28**, 1874–1883.
14 Y. E. Choi, K. H. Park, D. H. Kim, D. Y. Oh, H. R. Kwak, Y.-G. Lee and Y. S. Jung, *ChemSusChem*, 2017, **10**, 2605–2611.
15 Y. Ito, M. Otoyama, A. Hayashi, T. Ohtomo, A. Hayashi and M. Tatsumisago, *J. Power Sources*, 2017, **360**, 328−335.
16 Y. Ito, S. Yamakawa, A. Hayashi and M. Tatsumisago, *J. Mater. Chem. A,* 2017, **5**, 10658–10668.
17 J. Y. Kim, J. Kim, S. H. Kang, D. O. Shin, M. J. Lee, J. Oh, Y.-G. Lee and K. M. Kim, *ETRI Journal*, 2019, 1–9.
18 M. Otoyama, Y. Ito, A. Hayashi and M. Tatsumisago, *J. Power Sources*, 2016, **302**, 419–425.
19 M. Otoyama, Y. Ito, A. Hayashi and M. Tatsumisago, *Chem. Lett.*, 2016, **45**, 810–812.
20 K. Sugiura, H. Kubo, Y. Hashimoto and T. Koyama, *JP Patent Publication*, P2013–20894A.
21 N. Ohta, K. Takada, I. Sakaguchi, L. Zhang, R. Ma, K. Fukuda, M. Osada and T. Sakai, *Electrochem. Comm.*, 2007, **9**, 1486–1490.
22 M. Inaba, Y. Iriyama, Z. Ogumi, Y. Todzuka and A. Tasaka, *J. Raman Spectrosc.*, 1997, **28**, 613–617.
23 C. Julien and M. Massot, *Phys. Chem. Chem. Phys.*, 2002, **4**, 4226–4235.
24 Z. Liu, T. W. Verhallen, D. P. Singh, H. Wang, M. Wagemaker and S. Barnett, *J. Power Sources*, 2016, **324**, 358–367.

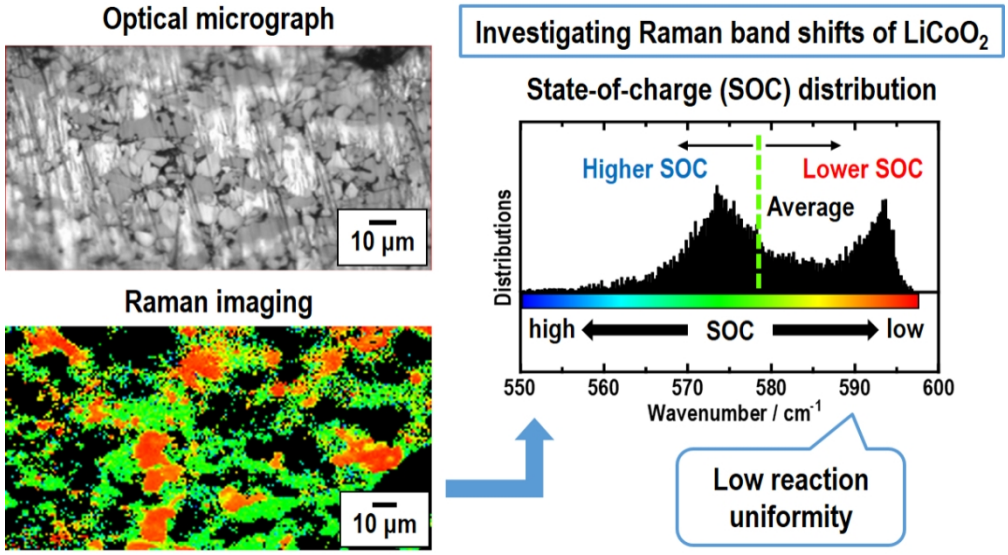

205x115mm (150 x 150 DPI)